Rarefaction-singular shock dynamics for conserved volume gravity driven particle-laden thin film

L. Wang*, A. Mavromoustaki, A. L. Bertozzi, G. Urdaneta, and K. Huang
Department of Mathematics, University of California Los Angeles,
520 Portola Plaza, Los Angeles, CA 90095, USA

(Dated: February 18, 2014)

We employ a recently proposed model [Murisic et. al, JFM 2013] to study a finite-volume, particle-laden thin film flowing under gravity on an incline. For negatively buoyant particles with concentration above a critical value, the similarity solution is of the rarefaction-singular shock type. We investigate the structure in detail and find that the particle/fluid front advances linearly to the *leading order* with time to the one-third power as predicted by the Huppert solution [Huppert, Nature 1982] for clear fluid (i.e. in the absence of particles). We also explore a deviation from this law when the particle concentration is high. Both results are carried over for the buoyant particles with any concentrations. We conduct several experiments with both buoyant and negatively buoyant particles whose results qualitatively agree with the theoretics.

I. INTRODUCTION

Mixtures of particles in viscous liquid, despite their wide range of industrial and geophysical applications [1, 2], have received far less attention than homogeneous flows [3, 4] and granular flows [5, 6]. Previous work has focused on sedimentation of a uniform suspension of particles in a quiescent bulk flow [7–9]. For gravitational transport of particles within a thin film of viscous oil, the authors in [10, 11] first derived a lubrication model considering the effects of gravity, capillarity and hindered settling. In a subsequent study [12, 13], the authors took into account the effect of shear-induced migration which successfully captured the three different regimes observed in physical experiments carried out using slurries composed of negatively buoyant particles. The three regimes are referred to as 'settled', where the particles settle to the substrate with clear fluid flowing over them, 'ridged', where the particles accumulate at the front of the flow and 'well-mixed', which is a transient, intermediate regime (see [13, 14] for more details). Recent experimental work [15] investigates the development of the above-mentioned regimes for bidisperse slurries composed of negatively buoyant particles, with one species being heavier than the other. The authors conclude that, in the 'settled' regime, they observe stratification of particles by densities, due to the dominant gravitational effects. For slurries composed of buoyant particles, only the 'ridged' regime is observed experimentally.

The front position, among the macroscopic flow features, is of paramount importance as it yields insight into the behavior of the various flow patterns. In [16], extensive experiments are carried out with qualitative trends suggesting that, although the presence of particles affects the geometry of the propagating front significantly, the measured average position versus time shows self-similar behavior as observed by Huppert [3] in the study of clear, thin films. For neutrally buoyant particles, [17] gives a detailed experimental study over a wide range of system parameters such as the particle concentration and the incline of the slope. The authors address the role the particle migration plays in the shape of the velocity profile as well as the good performance of the lubrication theory in predicting the fluid height and front position. A first attempt to analyze this observation is given in [18], wherein the role of the precursor is addressed for a homogeneous fluid, but the system of conservation laws describing the flow of slurry mixtures, especially in the high concentration limit, lacks analysis.

Our analysis shares some similarity with the work carried out by Grunewald *et al.* [18]. The authors employ a lubrication model for negatively buoyant particles, which does not incorporate all the relevant physics of the problem; this is evident by its failure to capture the existence of the 'settled' regime at low total particle concentrations. In the analysis presented in the current paper, we employ an 'equilibrium model' [13], which has shown excellent agreement with physical experiments. We consider constant volume initial data, for both negatively buoyant particles (focussing on the 'ridged' regime) and buoyant particles, which leads to a self-similar solution of rarefaction-singular shock type. We approximate the rarefaction

* Corresponding author. Email: liwang@math.ucla.edu

wave in concentration by its value at $\xi = 0$, where $\xi = \frac{x}{t}$, to the leading order, and recover the fact that the particle/fluid front position moves linearly with time to the one-third power. We also derive a general relationship between time and moving contact line without approximation, which shows a slight deviation from the one-third power law. The singular mass corresponding to the particle-rich ridge is shown to converge to a constant and we give an upper bound for it.

The rest of the paper is organized as follows. In Sec. II, we study in detail the rarefaction-singular shock structure for the two cases: (i) for negatively buoyant particles with concentration higher than the critical value and (ii) for buoyant particles. Since the latter case lacks analysis, we summarize the properties of its equilibrium model as well as the formation of the singular shock. In Section III, we discuss comparisons between experimental and theoretical results for suspensions composed of PDMS oil and small, noncolloidal particles. Concluding remarks are given in Section IV.

II. SIMILARITY THEORY

We use a theoretical model, derived in detail in [13], to describe the spatio-temporal evolution of a slurry mixture composed of silicon oil and noncolloidal particles. A schematic of the apparatus used in the experiments is shown in Fig. 1, where x is the axial flow direction, z is the direction normal to the flow and α denotes the plane angle of inclination. We note that the width of the plane is considered to be infinitely wide and, hence, any transverse effects are assumed to be negligible.

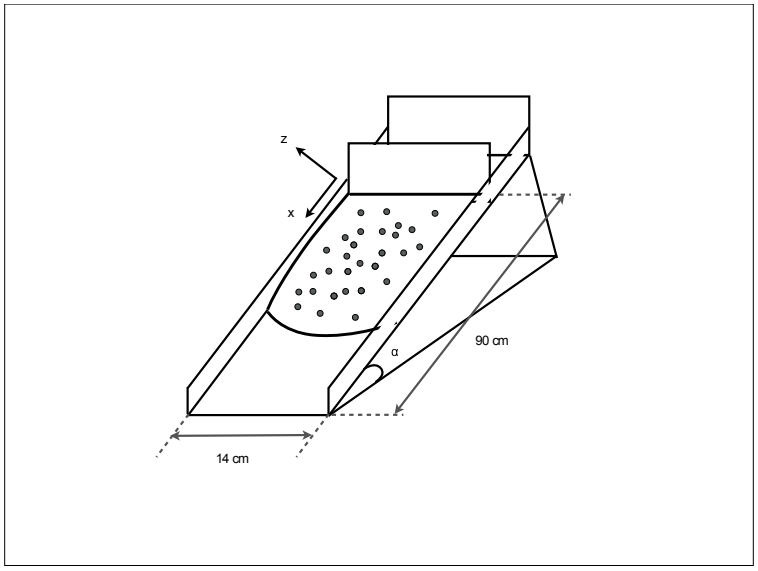

Figure 1: Schematic plot of the geometry of the setup.

The mathematical model consists of a 2×2 system of conservation laws which describe the evolution of the film thickness, $h(x,t)$, and integrated particle volume, $n(x,t)$, as follows:

$$h_t + \left(h^3 f\left(\phi_0\right)\right)_x = 0,\ n_t + \left(h^3 g\left(\phi_0\right)\right)_x = 0, \tag{1}$$

where $\phi_0(x,t) = \dfrac{n}{h} \in [0, \phi_{max}]$ is the particle volume fraction. Here ϕ_{max} is the particles' maximum packing fraction. Since the equilibrium equations are independent of the axial flow and time, we introduce a new variable $s = \frac{z}{h(t,x)}$ with $0 \leq s \leq 1$ to eliminate the implicit dependence on $h(x,t)$. The fluxes, $f\left(\phi_0\right) = \int_0^1 u(x,t;s)ds$ and $g\left(\phi_0\right) = \int_0^1 \phi(x,t;s)$, are a result of the equilibrium model for particle settling

and resuspension, which takes the following form:

$$\begin{cases} \left(1 + C_1 \dfrac{\phi}{\phi_{max} - \phi}\right) \sigma\phi' + C_2 - (C_2 + 1)\phi - \rho_s \phi^2 = 0, & \text{(2a)} \\ \sigma' = -(1 + \rho_s \phi), & \text{(2b)} \\ \sigma(1) = 0, & \text{(2c)} \\ \sigma(0) = 1 + \rho_s \phi_0(x, t). & \text{(2d)} \end{cases}$$

Here $\rho_s = \frac{\rho_{par} - \rho_{liq}}{\rho_{liq}}$, $C_1 = \frac{2(K_v - K_c)}{K_v}$, $C_2 = \frac{2\rho_s \cot\alpha}{9K_c}$ and $\sigma(x, t; s)$ is the shear stress. The equilibrium model (2) gives solutions for $\phi(s)$ and $\sigma(s)$ which need to be updated at every point in x. Using the aforementioned equilibrium solutions, we construct the suspension velocity u as follows:

$$u'(x, t; s) = \frac{\sigma(x, t; s)}{\mu\left(\phi(x, t; s)\right)}, \qquad u(x, t; 0) = 0. \tag{3}$$

This model, derived systematically on an equilibrium theory [13], applies to both buoyant and negatively buoyant particles with different parameters. For negatively buoyant particles, the equilibrium system (2) has an unstable critical value for the particle concentration, which leads to three different regimes observed in the experiments: settled (< critical value), mixed (=critical value) and ridged (> critical value). The three regimes are shown in Fig. 2 for negatively buoyant particles.

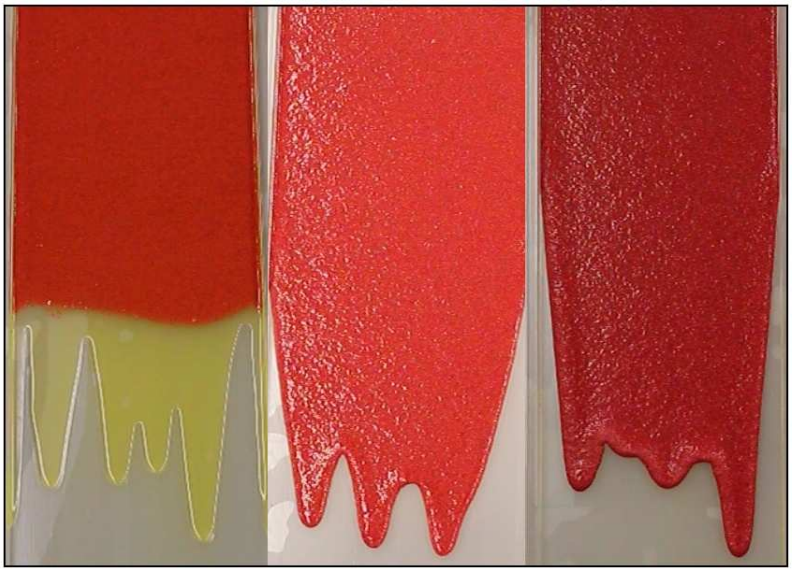

Figure 2: Flow regime patterns emerging from a fixed volume of silicon oil laden with negatively buoyant beads. Here, the particle volume fraction is fixed at 0.40 while the plane angle of inclination is varied from 15° (left) to 30° (middle) to 45° (right) corresponding to the 'settled', 'well-mixed' and 'ridged' regime, respectively. In the 'settled' regime, clear fluid (shown in yellow) flows over the particle-rich fluid while in the 'ridged' regime, the particles accumulate at the front forming a particle-rich ridge. The middle panel shows an intermediate regime where the particles remain well mixed in the fluid. The images show the patterns at their fully developed state. The experiments were run in the Applied Mathematics Laboratory at University California, Los Angeles (UCLA).

Some analysis for these different regimes are available in [19], and also in [20] with emphasis on the exploration of singular shock in ridged regime. For buoyant particles, it is shown that all particles move to the free surface and form a particle-rich ridge for any value of the particle concentration.

A. Negatively buoyant particles

In this section, we consider the flow of a mixture of oil and negatively buoyant particles described mathematically by Eqs. (1)–(2) with conserved volume initial data

$$h(0,x) = \begin{cases} h_I, & \text{for } 0 \le x \le x_I = 1, \\ 0, & \text{elsewhere,} \end{cases} \qquad \phi_0(0,x) = \phi_I, \quad n(0,x) = \phi_I h(0,x). \tag{4}$$

Here, we focus on the high concentration case, i.e., $\phi_I > \phi_{crit}$. Figure 3 shows the numerical solution using the initial data given by Eq. (4) [shown in panel (a)]. In panel (b), we show the solution for h and n at $t = 65$ characterized by a shock followed by a rarefaction. Finally, in panel (c), we show the solution for the particle volume fraction, ϕ_0 at $t = 65$.

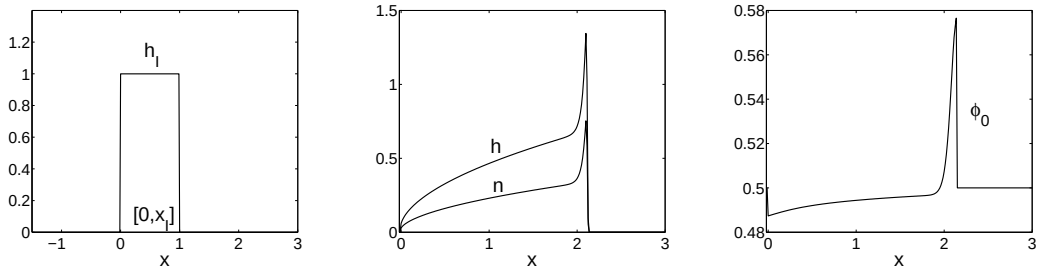

(a) (b) (c)

Figure 3: (a) Initial profile for h representing a finite volume setup. (b) Numerical solution for h and n at $t = 65$. (c) Numerical solution for ϕ_0 at $t = 65$. The plane angle of inclination was chosen as $\alpha = 30^o$ and the initial total volume fraction was set to $\phi_0 = 0.5$.

The shock dynamics have been extensively studied in [10, 19, 20], while the analysis for rarefaction is briefly mentioned in [19]. Here, we begin our discussion with the rarefaction theory. The Jacobian of the hyperbolic system (1) is given by

$$J = h^2 \begin{pmatrix} 3f - \phi_0 f' & f' \\ 3g - \phi_0 g' & g' \end{pmatrix} := h^2 \tilde{J}. \tag{5}$$

For a given state (h_I, n_I), the sets of the states (h_r, n_r) that can be connected to (h_I, n_I) by a rarefaction curve lie on the integral curve, which is defined as $\begin{pmatrix} h_r'(\xi) \\ n_r'(\xi) \end{pmatrix} = \frac{\tilde{r}_i(\phi_r)}{\nabla\left(h_r^2 \tilde{\lambda}_i(\phi_r)\right)\cdot \tilde{r}_i(\phi_r)}$, $i = 1,\ 2$, where $\tilde{\lambda}_i$ and $\tilde{r}_i$ are the eigenvalues and corresponding eigenvectors for $\tilde{J}$. A typical plot of the integral curve for a given right state $(h_R, n_R) = (1, 0.5)$ is displayed in Fig. 4, where the dashed curve refers to the 1-wave and solid curve refers to the 2-wave.

Figures 3 and 4 suggest that the solution for system (1)–(2) with initial data (4) is a 2-rarefaction following a singular shock. Therefore, the rarefaction wave $(h_r(\xi), n_r(\xi))$ takes the form

$$\begin{pmatrix} h_r'(\xi) \\ n_r'(\xi) \end{pmatrix} = \frac{\tilde{r}_2(\phi_r)}{\nabla\left(h_r^2 \tilde{\lambda}_2(\phi_r)\right)\cdot \tilde{r}_2(\phi_r)} = \frac{\tilde{r}_2(\phi_r(\xi))}{h_r(\xi)\left(2\tilde{\lambda}_2(\phi_r) - \phi_r \tilde{\lambda}_2'(\phi_r), \tilde{\lambda}_2'(\phi_r)\right)\cdot \tilde{r}_2(\phi_r(\xi))}, \tag{6}$$

with the right boundary condition

$$h_r\left(\frac{x_{liq}}{t}\right) = h_{liq}, \quad n_r\left(\frac{x_{par}}{t}\right) = n_{par}, \tag{7}$$

where the subscripts 'liq' and 'par' represent liquid and particle, respectively. Here $\tilde{\lambda}_2$ and $\tilde{r}_2$ represent the larger eigenvalue and corresponding eigenvector to matrix $\tilde{J}$.

We claim that the solution to (6)–(7) satisfies $h_r(0) = 0$, $n_r(0) = 0$. This is obtained by noticing that the rarefaction wave satisfies the relation $\xi = \frac{x}{t} = h_r^2(\xi)\tilde{\lambda}_2(\phi_r(\xi))$, where $h_r^2(\xi)\tilde{\lambda}_2(\phi_r(\xi))$ is the eigenvalue

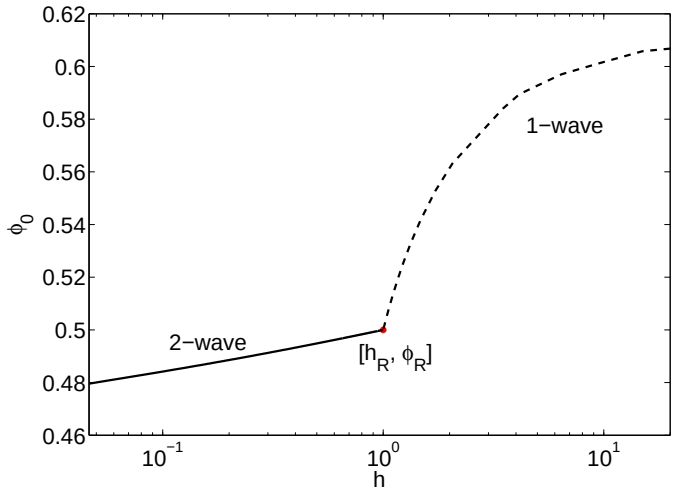

Figure 4: Rarefaction integral curve for a given right state $(h_R, \phi_R) = (1, 0.5)$ (shown by a circle marker). The dashed curve refers to the 1-wave and the solid curve refers to the 2-wave.

of system (1) and $\tilde{\lambda}(\phi_r(\xi))$ is checked to be nonzero, thus $h_r(\xi = 0) = 0$. Moreover, if $n_r(0) \neq 0$, we have $\phi_r(0) = \frac{n_r(0)}{h_r(0)} = \infty$, which is physically unrealistic.

Next, we compute $\phi_r(0)$ using

$$\phi_r(0) = \frac{n_r'(0)}{h_r'(0)} = \frac{r_2^{(2)}(\phi_r(0))}{r_r^{(1)}(\phi_r(0))} = \frac{\tilde{\lambda}_2(\phi_r(0)) - (3f(\phi_r(0)) - \phi_r(0)f'(\phi_r(0)))}{f'(\phi_r(0))}, \tag{8}$$

by noting that $n_r'(0) = h_r'(0)\phi_r(0)$. Therefore, $\tilde{\lambda}_2(\phi_r(0)) = 3f(\phi_r(0))$ and thus $\phi_r(0) = \phi_{crit}$. Now, *approximate ϕ_0 at the leading order:* ξ near 0, i.e., $\phi_r(\xi) \simeq \phi_r(0)$, (6) becomes

$$h_r'(\xi) \simeq \frac{1}{h_r(\xi)} \frac{r_2^{(1)}(\phi_r(0))}{\left(2\tilde{\lambda}_2(\phi_r(0)) - \phi_r(0)\tilde{\lambda}_2'(\phi_r(0)), \tilde{\lambda}_2'(\phi_r(0))\right) \cdot r_2(\phi_r(0))} := \frac{1}{h_r(\xi)} A, \tag{9}$$

$$n_r'(\xi) \simeq \frac{1}{n_r(\xi)} \frac{r_2^{(2)}(\phi_r(0))\phi_r(0)}{\left(2\tilde{\lambda}_2(\phi_r(0)) - \phi_r(0)\tilde{\lambda}_2'(\phi_r(0)), \tilde{\lambda}_2'(\phi_r(0))\right) \cdot r_2(\phi_r(0))} := \frac{1}{n_r(\xi)} B, \tag{10}$$

therefore

$$h_r(\xi) \simeq \sqrt{2A}\sqrt{\xi}, \qquad n_r(\xi) \simeq \sqrt{2B}\sqrt{\xi}. \tag{11}$$

The singular shock formation for negatively buoyant particles with high concentration is well studied in [20]. In the presence of the singularity at the wave front, the mass of the mixture and particles (h and n) accumulate in the singular region, and the accumulation rate satisfies the generalized Rakine-Hugoniot condition [21]. More precisely, we define the singular mass as

$$M_h(t) = \int_{|x-st|<\delta} h(t,x)dx, \quad M_n(t) = \int_{|x-st|<\delta} n(t,x)dx, \tag{12}$$

where s is the shock speed. Then, the growth rate satisfies

$$\frac{dM_h}{dt} = s[h] - \left[h^3 f\left(\frac{n}{h}\right)\right], \quad \frac{dM_n}{dt} = s[n] - \left[h^3 g\left(\frac{n}{h}\right)\right]. \tag{13}$$

where $[\star] = \star_R - \star_L$. Now, using the conservation of mass, we have

$$t\int_0^{\frac{x_s}{t}} \sqrt{2A}\sqrt{\xi}d\xi + M_h(t) = h_I x_I, \tag{14}$$

$$t\int_0^{\frac{x_s}{t}} \sqrt{2B}\sqrt{\xi}d\xi + \phi_{max}M_h(t) = \phi_I h_I x_I, \tag{15}$$

for any t, and $x_s(t)$ is the shock position. Here, we make use of the fact that the singular mass in n and h satisfy the relationship $M_n(t) = \phi_{max}M_h(t)$ as explained in [20]. Notice that when $\phi_r(0) = \phi_{crit}$, the 2-eigenvalue and 2-eigenvector is $\lambda_2 = 3f(\phi_{crit})$, $r_2 = (1 \;\; \phi_{crit})^T$. Therefore, $B = \phi_{crit}^2 A$, and the following relations are satisfied

$$M_h(t) = \frac{(\phi_I - \phi_{crit})h_I x_I}{\phi_{max} - \phi_{crit}}, \quad x_s = \left(\frac{(\phi_{max} - \phi_I)h_I x_I}{\frac{2}{3}\sqrt{2A}(\phi_{max} - \phi_{crit})}\right)^{\frac{2}{3}} t^{\frac{1}{3}} := C_s^0 t^{\frac{1}{3}}. \tag{16}$$

Further simplification leads to

$$x_s = \left[(1 + \rho_s\phi_{crit})\left(1 - \frac{\phi_I}{\phi_{max}}\right)^2 \frac{9h_I^2 x_I^2}{4}\right]^{\frac{1}{3}} t^{\frac{1}{3}}, \tag{17}$$

where we use the fact that $A = \frac{1}{6f(\phi_{crit})}$ obtained from (9). This is reminiscent of Huppert's formula for the clear fluid [3], which may be applied to the *well-mixed* particle-laden flow with concentration ϕ_I, such that

$$x_s = \left[(1 + \rho_s\phi_I)\left(1 - \frac{\phi_I}{\phi_{max}}\right)^2 \frac{9h_I^2 x_I^2}{4}\right]^{\frac{1}{3}} t^{\frac{1}{3}}. \tag{18}$$

Then a comparison of (17) and (18) implies that the effects of particle settling and resuspension slow down the advancing flow a little bit. Another observation is that the coefficient in (17) decreases as ϕ_I increases, which is consistent with the experimental results discussed by Ward *et al.* [16]. We have shown the particle (liquid) front position versus time$^{\frac{1}{3}}$ in Fig. 5(a), where the solid line is obtained by solving the system of conservation laws (1) and the dashed line has a slope given by (17). We observe that (17), is somewhat underestimated due to the approximation (11) being only accurate to the leading order.

In fact, we can have a more precise result without doing the approximation. The shock position satisfies the following relation due to the singular shock speed formula in [20]:

$$x_s'(t) = \frac{\phi_{max}h_r^3(\xi)f(\phi_r) - h_r^3(\xi)g(\phi_r)}{\phi_{max}h_r - h_r\phi_r} = \frac{\phi_{max}f(\phi_r) - g(\phi_r)}{(\phi_{max} - \phi_r)\tilde{\lambda}_2(\phi_r)}\frac{x_s}{t} := P_c\frac{x_s}{t}, \tag{19}$$

where we have used relation $\xi = \frac{x}{t} = h_r^2(\xi)\tilde{\lambda}_2(\phi_r(\xi))$. This implies $x_s(t) \propto t^{P_c}$, where P_c is given in Fig. 5. Here, one observes that P_c is around $\frac{1}{3}$ for $\phi_0 > \phi_{crit}$. Then, the conservation of mass

$$t\int_0^{\frac{x_s}{t}} h_r(\xi)d\xi + M_h(t) = h_I x_I, \quad t\int_0^{\frac{x_s}{t}} n_r(\xi)d\xi + \phi_{max}M_h(t) = h_I x_I\phi_I$$

gives rise to $h_r(\xi) \propto \xi^\alpha$ and $n_r(\xi) \propto \xi^\alpha$ with $\alpha = \frac{P_c}{1-P_c}$. Moreover, we obtain the form of the singular mass: $M_h(t) = \frac{\phi_I - \phi_r}{\phi_{max} - \phi_r}h_I$ with $\phi_r \in [\phi_{crit}, \phi_I]$, which implies the following upper bound

$$0 \le M_h(t) \le h_I \min\left\{\frac{\phi_I - \phi_{crit}}{\phi_{max} - \phi_{crit}},\ \phi_I\right\}. \tag{20}$$

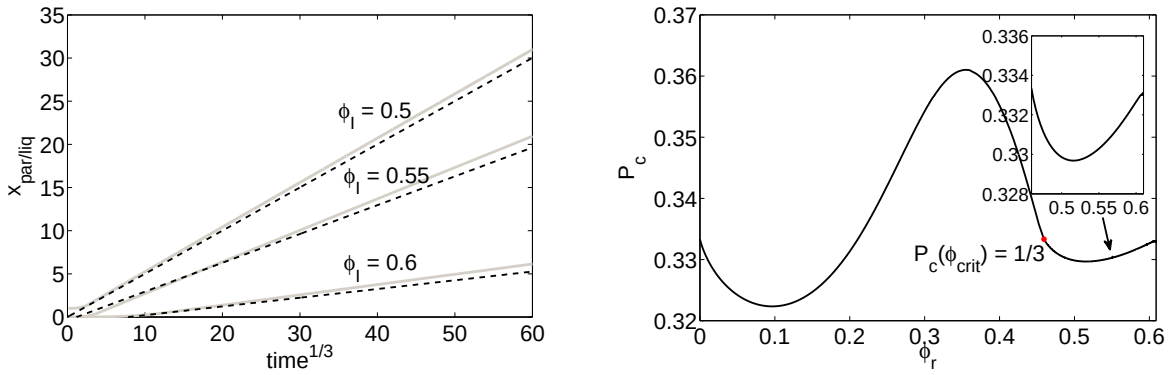

(a) (b)

Figure 5: (a) Plots of position $x_{par/liq}$ versus $time^{1/3}$ for different concentration $\phi_0 = 0.5,\ 0.55,\ 0.6$. Grey solid lines: numerical simulation of (1). Black dash lines: slope calculated from (16). (b) Plots of P_c in (19). The plane angle of inclination was chosen as $\alpha = 30^\circ$.

B. Buoyant particles

In this section we consider suspensions with buoyant particles. The model for particle suspension remains the same as in (1)–(2) but with different parameters: $\rho_s = \frac{\rho_{par}-\rho_{liq}}{\rho_{liq}} < 0$. Then, $C_1 = \frac{2(K_v-K_c)}{K_v} > 0$, $C_2 = \frac{2\rho_s \cot\alpha}{9K_c} < 0$. It is easy to check that for $\phi \in [0, \phi_{max}]$, $\rho_s\phi^2 + (C_2+1)\phi - C_2 > 0$ for any angle $\alpha \in [0, 90^\circ]$, thus there is no critical point for this case, contrary to the negatively buoyant case. Moreover, since $\phi' > 0$, we have $g(\phi_0) \geq f(\phi_0)\phi_0$, i.e., any $\phi_0 \in [0, \phi_{max}]$ leads to a particle-rich ridge. Figure 6 gives a typical plot of particle volume fraction ϕ, shear stress σ and suspension velocity u for $\alpha = 30^\circ$. It is interesting to point out that the shape of velocity u is blunting in contrast to the parabolic profile for homogeneous Newtonian fluids, which is in good agreement with the experimental observation in [17]. Figure 7 compares the fluxes $f(\phi_0)$ and $g(\phi_0)$ for buoyant and negatively buoyant particles for $\alpha = 30^\circ$.

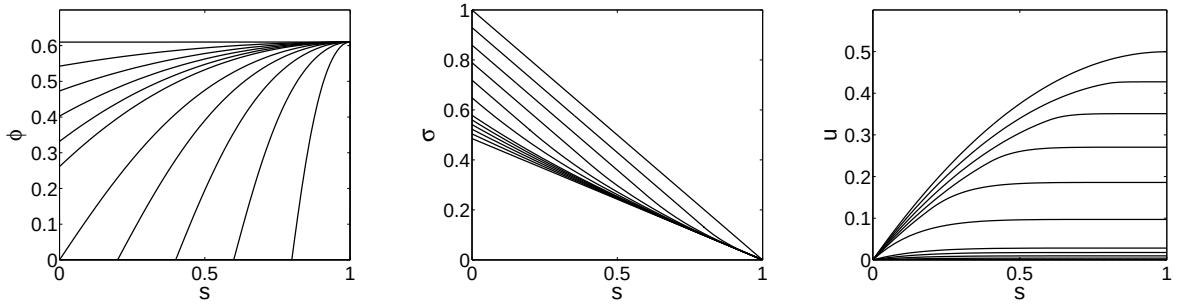

(a) (b) (c)

Figure 6: Plots of solutions to (2) for $\alpha = 30^\circ$. The horizontal axis represents the s variable. Different curves refer to different initial data ϕ_0. In panels (a), (b) and (c), we show the particle volume fraction ϕ, shear stress σ and suspension velocity u, respectively.

1. *Singular shock formation*

Since the formation of the singular shock for buoyant particles is similar to the negatively buoyant case with high particle concentration, the results in [20] may be applied here with a slight change to fit the buoyant parameters. Figure 8 shows the Hugoniot loci for left and right states ($h_L = 1, \phi_I = 0.3$) and

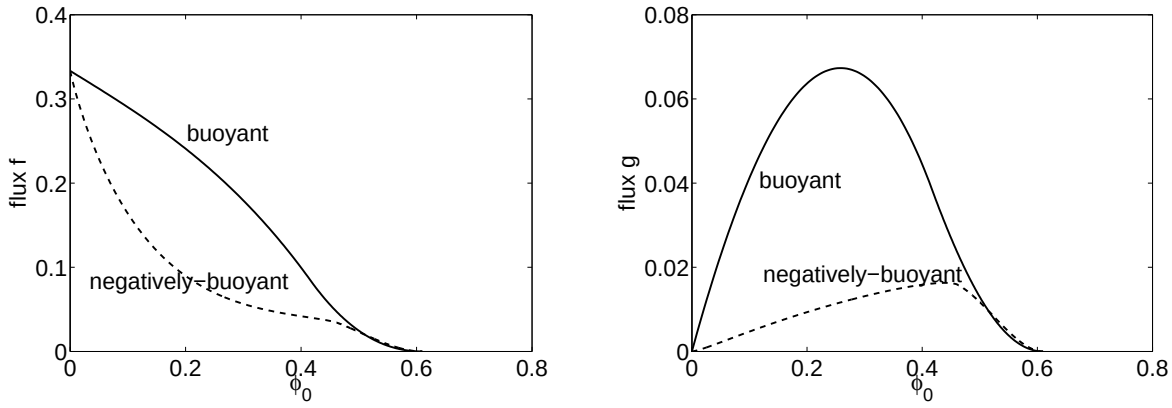

(a) (b)

Figure 7: Fluxes f [panel (a)] and g [panel (b)] for buoyant and negatively-buoyant cases. The plane angle of inclination is set to $\alpha = 30^\circ$.

$(h_R = 0.01, \phi_I = 0.3)$, we observe that these two curves are *asymptotically parallel* and thus give rise to a singular shock. Denote

$$\begin{aligned} B &= \frac{\rho_s \phi_{max}^2 + (C_2+1)\phi_{max} - C_2}{C_1 \phi_{max}(1+\rho_s \phi_{max})}, \\ \theta &= \arccos\left(1 + \frac{3B^2(2B+3)\phi_{max}^2 \mu_l}{2(\phi_{max}-\phi_L)^3(1+\rho_s\phi_{max})(1+B)^4}\left(g(\phi_I) - \phi_{max} f(\phi_I)\right)\right), \end{aligned}$$

then, for a given left state (h_L, ϕ_I), we have the threshold value $h_R^* = h_L \frac{1-\cos\frac{\theta}{3}+\sqrt{3}\sin\frac{\theta}{3}}{1+2\cos\frac{\theta}{3}}$ in the sense that when $h_R \le h_R^*$ there is a singular shock and when $h_R > h_R^*$ a double shock emerges. Moreover, the singular shock speed is $s = \frac{(h_L^2+h_R^2+h_L h_R)(\phi_{max} f(\phi_I) - g(\phi_I))}{\phi_{max}-\phi_I}$. The reader is referred to [20] for more details.

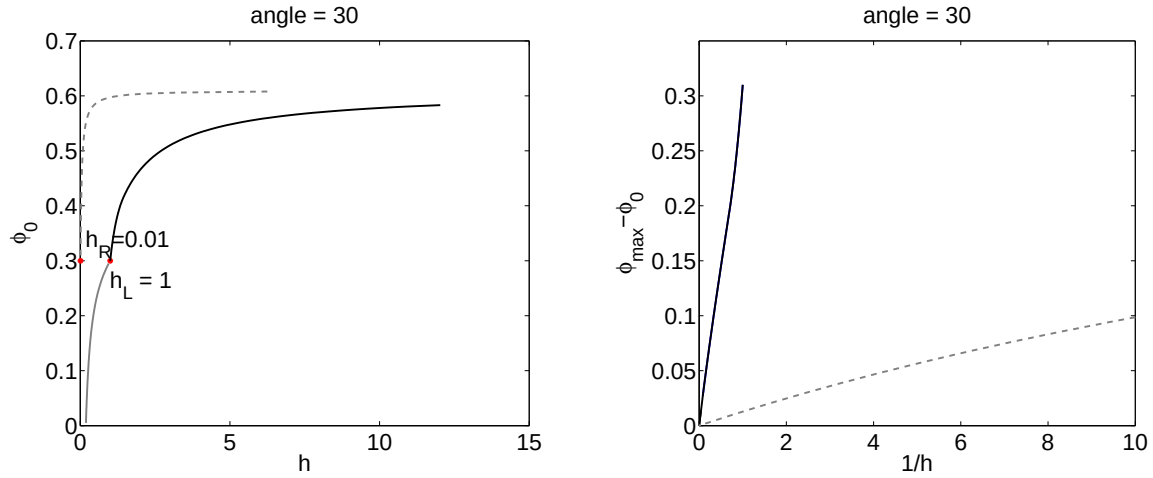

(a) (b)

Figure 8: (a) The entropy-satisfying shocks connecting the left state $(h_L, \phi_L) = (1, 0.3)$ (black curves) and right state $(h_R, \phi_R) = (0.01, 0.3)$ (grey dashed curves). (b) Replotted Hugoniot loci from panel (a) with vertical axis representing $\phi_{max} - \phi_0$ and horizontal axis representing $\frac{1}{h}$. The plane angle of inclination is $\alpha = 30^\circ$.

2. Rarefaction-singular shock solution

By analogy with the negatively buoyant case, we first approximate $\phi_r(\xi)$ by $\phi_r(0)$ near $\xi = 0$, then we can compute $\phi_r(0)$ as in (8), and get $\phi_r(0) = 0$ in this case. A similar approach in (9)–(15) applies and yields the relationship between particle front position and time as in (16). This relation is shown in Fig. 9(a), where the black line is obtained by solving the hyperbolic conservation laws and the dashed line has the slope in (16). We can also derive the relations between time and shock position similarly using (19) but with f and g for the buoyant case. A typical plot of P_c is given in Fig. 9(b) for $\alpha = 30°$. It is again shown that P_c is in the neighborhood of $\frac{1}{3}$. As a result, the singular mass has the same estimate (20).

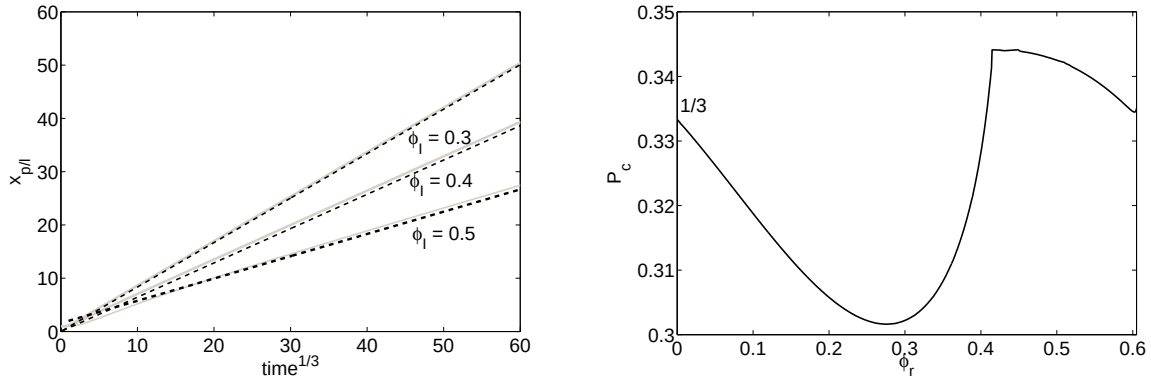

(a) (b)

Figure 9: (a) Plots of position $x_{par/liq}$ versus time$^{1/3}$ for different values of concentration: $\phi_I = 0.3,\ 0.4,\ 0.5$. Grey solid lines: numerical simulation of (1); black dash lines: slope calculated from (16). (b) Plots of P_c in (19) for the buoyant case. Again, $\alpha = 30°$.

We also compare the particle front position versus time through Eq. (17) for negatively buoyant and buoyant cases. The results are shown in Fig. 10; it is observed that these qualitatively agree with the experimental results in [16] and [17]. The comparison with Huppert's formula (18) is also presented. Here, we conclude that in the presence of particle setting and resuspension, if the particles are negatively buoyant, the speed of the slurry mixture is decreased, while, on the other hand, if the particles are buoyant, the speed of the slurry mixture is increased.

III. EXPERIMENTS

A. Procedure

In this section, we provide details of the experimental setup and procedure. A schematic of the apparatus is shown in Fig. 1; it consists of an acrylic track of length 90 cm and width 14 cm with an inclination angle, α, where the latter may be adjusted within $5° < \alpha < 80°$. In the experiments we carry out, we are interested in the flow patterns that emerge from gravity-driven fslurry flows composed of PDMS oil and noncolloidal beads. Two types of beads are used: negatively buoyant (approximately 2.5 times heavier than the fluid) and buoyant (approximately 0.6 times lighter than the fluid). The two system parameters we are interested in are α and the total particle volume fraction, ϕ_I. Slurry mixtures of 100 ml total volume are prepared for different values of ϕ_I and deposited in the reservoir with the release gate initially closed. The start of each run is marked at the point when the gate is lifted. The slurry mixture subsequently flows down the track and the motion is recorded using a digital camera until the front of the flow reaches the end of the track. The runs are repeated 2-3 times to validate the experimental results. The experimental parameters used are summarized in Table I.

In the case of negatively buoyant particles, we observe three distinct regimes, depending on the particle volume fraction, as shown in the work of Murisic *et al.* [13, 14]. As discussed in Section II, the equilibrium

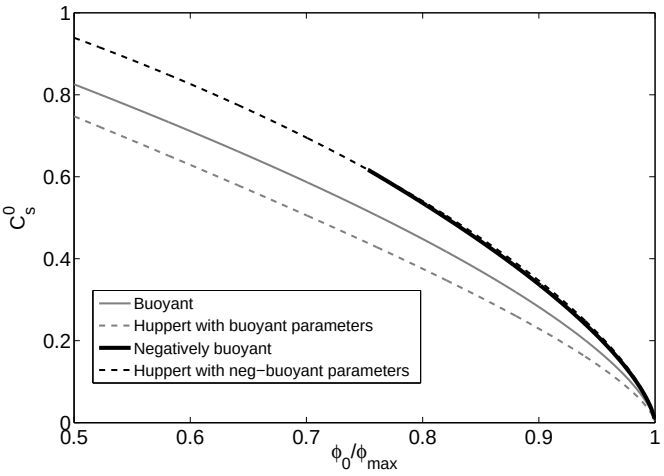

Figure 10: Plots of C_s^0, obtained using Eq. (16) against $\frac{\phi_0}{\phi_{max}}$. Grey solid curve: buoyant case; black solid curve: negatively buoyant case. Grey dashed curve: Huppert formula (18) with buoyant parameters; black dashed curve: Huppert formula with negatively buoyant parameters. Again, $\alpha = 30^\circ$.

model exhibits an unstable critical value for the particle volume fraction, denoted by ϕ_{crit}. While the slurry mixture starts off as 'well-mixed', within $0 < \phi < \phi_{crit}$, gravitational settling dominates thus clear fluid flows over particles which settle fast to the substrate. Within $\phi_{crit} < \phi < \phi_{\max}$, competition between gravitational settling and shear-induced migration, leads to the particles accumulating at the front of the flow forming a particle-rich ridge. As previously discussed, the two regimes are termed 'settled' and 'ridged', respectively. In this section we are interested in making comparisons between experimental and theoretical results focussing on the 'ridged' regime. The reader is referred to previous work [13, 14] for comparisons within the 'settled' regime.

Table I: Experimental parameters used

particles	d (mm)	ρ_p (kg/m^3)
Glass, negatively buoyant	0.25-0.50	2500
Glass, buoyant	0.25-0.55	640

fluid	ν (m^2/s)	ρ_l (kg/m^3)
PDMS oil	10^{-3}	970

B. Comparison between experimental results & theoretical predictions

In Fig. 11 we show a series of static images of the slurry mixtures flowing down the plane with the angle of inclination fixed at $\alpha = 40^\circ$. The pictures show a comparison between the evolution of the flow patterns for the cases of buoyant particles (pink slurry flows) and negatively buoyant particles (red slurry flows). Figure 11 depicts the flow patterns initially [panels (a), (b)], when the slurries have travelled approximately half way down the plane [panels (c), (d)] and in their fully developed patterns [panels (e), (f)]. The different times corresponding to each panel are included in the figure caption. We observe that for both particle species, the flow patterns develop in the 'ridged' regime where the majority of particles accumulate at the front of the flow hence the particle and fluid fronts coincide. We note that for the set of system parameters shown in Fig. 11, the slurry made of negatively buoyant particles traveled the same distance in approximately a third of the time.

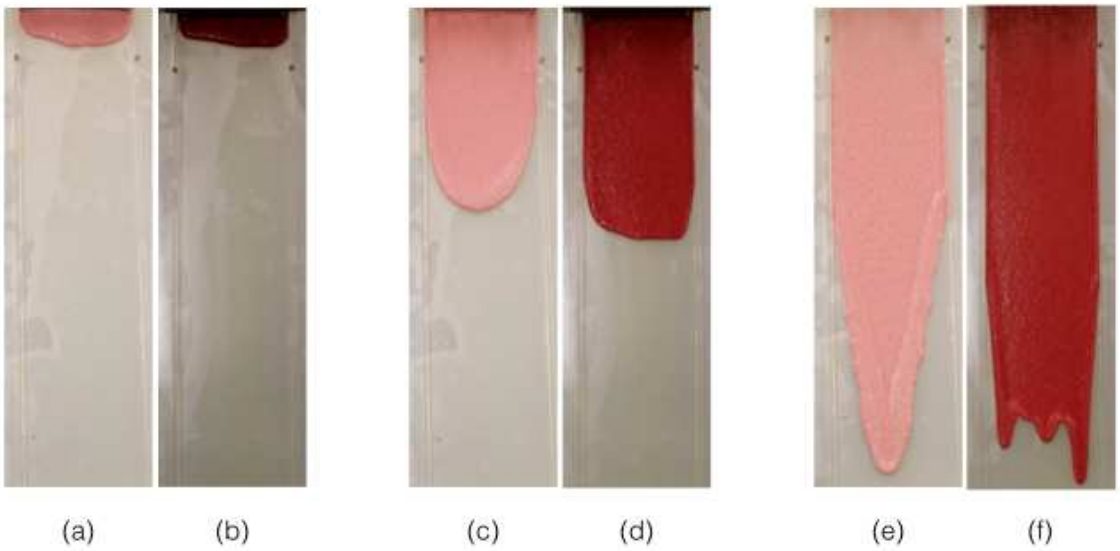

Figure 11: Static images for buoyant (pink) and negatively buoyant (red) slurries flowing down the plane inclined at $\alpha = 40^\circ$. The total particle concentration for both slurry mixtures is fixed at $\phi_I = 0.40$. The images of the buoyant slurry mixtures are captured at $t = 13$, 125, 625 seconds [shown in panels (a), (c), (e)] while the negatively buoyant slurry mixtures are captured at $t = 4$, 46, 237 seconds [shown in panels (b), (d), (f)].

In Figs. 12 and 13, we compare the theoretical prediction of the relationship between the fluid/particle front and time$^{1/3}$ [given by Eq. (17)] to the experimental results for negatively buoyant and buoyant beads, respectively. Figure 12 depicts the results using negatively buoyant particles for an angle of inclination of 40° [panel (a)] and 50° [panel (b)] for $\phi_I = 0.50, 0.55$. We observe that, after an initial transient time, wherein the mixture moves from the initial well-mixed state to the 'ridged' regime, the relation of the moving front with time$^{1/3}$ shows good agreement between the theoretical and experimental results. Figure 13 shows the relationship between the theoretical prediction and experimental results for buoyant particles. The experiments are carried out for two angles of inclination: 30° [panel (a)] and 40° [panel (b)] at $\phi_I = 0.30, 0.40$. As previously mentioned, in the case of buoyant particles any ϕ_I within $0 < \phi_I < \phi_{\max}$ results in the development of the 'ridged' regime leading to the two fronts (liquid and particle) coinciding. We observe a longer initial transient time compared to the negatively buoyant case. At late times, while the theoretical prediction approaches the slope of the experimental results, we note that the agreement is not as good as in the results shown in Fig. 12. A possible reason for this behavior is given by the experimental images shown in Fig. 11: for the buoyant particles (pink slurry flows), we observe the presence of significant wall boundary effects. The beads advance to the front and concentrate in the middle of the plane. Since the theoretical prediction is based on a one-dimensional model, a more uniform averaged front is expected to compare more closely to theoretical predictions. It can be observed in Fig. 11, that the averaged front of the flow in the case of negatively buoyant particles (red slurry flows) is more uniform compared to the buoyant case.

IV. CONCLUDING REMARKS

This paper focuses on the 'ridged' regime observed in the gravitational flow of a finite-volume, particle-laden thin film down a rectangular plane. In the case of slurries composed of negatively buoyant particles, this regime is observed experimentally at high particle concentrations and high angles of inclinations while for buoyant particles, the 'ridged' regime is the dominant flow pattern. In this paper we use a previously derived model [13] based on the lubrication approximation and the assumption that the particle distribution in the normal direction to the plane is in equilibrium.

We discuss our findings for slurries made up of both negatively buoyant particles (approximately 2.5 times heavier than the fluid) and buoyant particles (approximately 0.6 times lighter than the fluid). In both

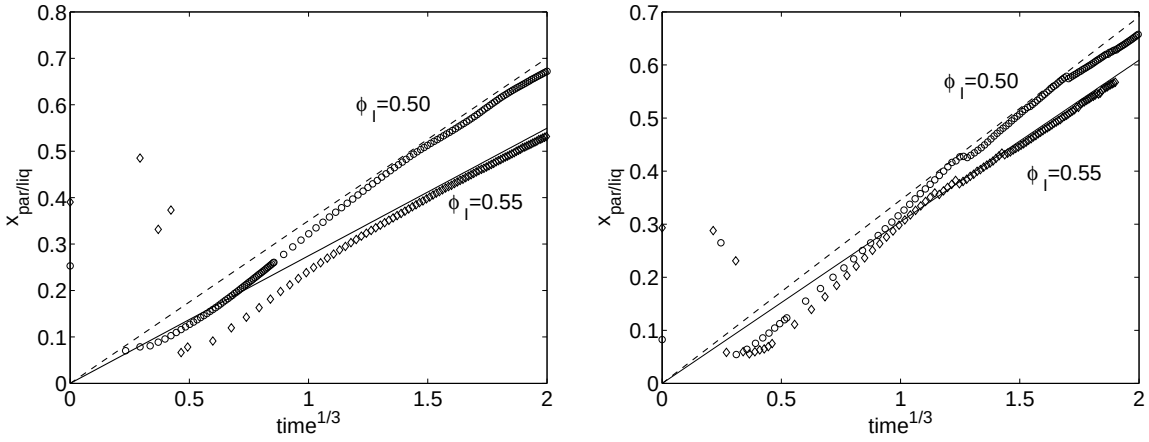

Figure 12: Comparison of experimental results against the theoretical formula given by Eq. (17) on the relationship of the location of the front, $x_{par/liq}$ and time$^{1/3}$. In panel (a), α is set at 40° while in (b), $\alpha = 50°$. In both panels, the particle concentration is varied from $\phi_I = 0.50$ (experiment: circle markers, theory: dashed line) to $\phi_I = 0.55$ (experiment: diamond markers, theory: solid line). For all system parameters shown, the experimentally observed flow pattern was within the 'ridged' regime.

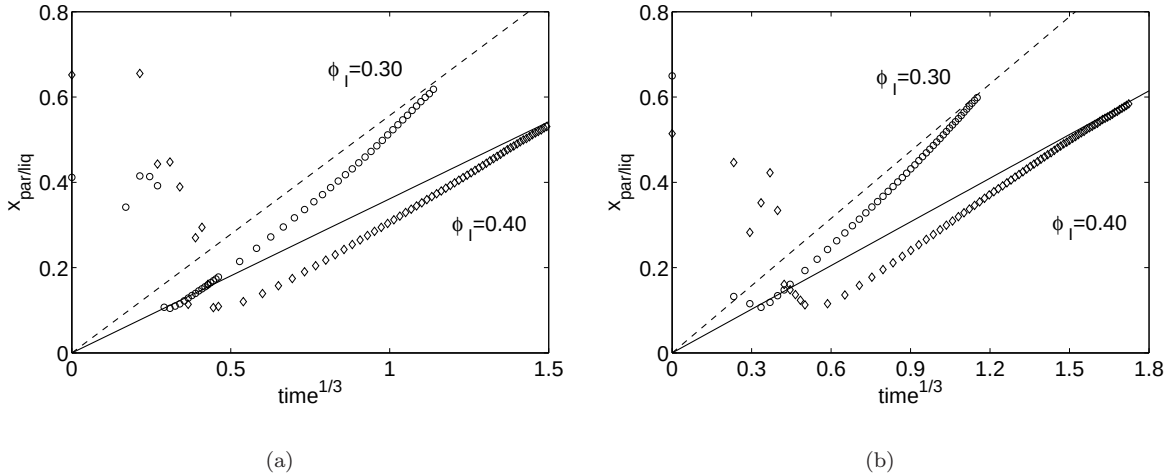

Figure 13: Comparison of experimental results against the theoretical formula given by Eq. (17) on the relationship of the location of the front, $x_{par/liq}$ and time$^{1/3}$ for buoyant particles. The plane angle of inclination α is set at 30° and the particle concentration is varied from $\phi_I = 0.30$ to $\phi_I = 0.40$.

cases, the solution is described by a rarefaction-singular shock. In the long time scaling, we approximate the rarefaction wave at its leading order and find that the particle/fluid front moves linearly with time to the one third power. This is reminiscent of Huppert's result for clear fluid [3]. We also derive a general relationship between the moving wave front and time which reveals some deviation form the one third power law. This coincides with the experimental observations in [16].

Next, we carry out experiments to investigate how the time-dependent relationship of the front of the flow obtained theoretically, compares against physical results. For the heavy particles, we choose particle concentrations that exceed the critical value to ensure the flow patterns are in the 'ridged' regime. It is noted that all slurry runs start off from a 'well-mixed' state. We carry out a series of experiments at two different angles: 40° and 50° (negatively buoyant) and 30° and 40° (buoyant) and two different particle

concentrations, $\phi_I = 0.50$ and $\phi_I = 0.55$ (negatively buoyant) and $\phi_I = 0.30$ and $\phi_I = 0.40$ (buoyant). We find that, after an initial transient period, the front of the flow shows a linear relationship with time$^{1/3}$ which approaches the slope of the formula obtained theoretically. For the negatively buoyant particles, the good agreement between experiments and theory is consistent. For the buoyant particles, we observe a longer initial transient period and, while we recover a linear relationship between $x_{\text{par/liq}}$ and time$^{1/3}$, the agreement is not as good as in the negatively buoyant case due to significant wall boundary effects.

Acknowledgements

This work was supported by UC Lab Fees Research Grant 09-LR-04-116741-BERA and NSF grants DMS-1048840 and DMS-1045536. The authors would like to acknowledge Mr. Matthew Hin and Mr. Shreyas Kumar for their valuable contribution to this paper.

[1] O. Katz and E. Aharonov. Landslides in vibrating sand box: What controls types of slope failure and frequency magnitude relations? *Earth Planet. Sci. Lett.*, 247:280–294, 2006.
[2] A. Klar, E. Aharonov, B. Kalderon-Asael, and O. Katz. Analytical and observational relations between landslide volume and surface area. *Journal of Geophysical Research: Earth Surface*, 116, 2011.
[3] H. E. Huppert. Flow and instability of a viscous current down a slope. *Nature*, 300:427–429, 1982.
[4] M. F. G. Johnson, R. A. Schluter, M. J. Miksis, and S. G. Bankofft. Experimental study of rivulet formation on an inclined plate by fluorescent imaging. *J. Fluid Mech.*, 394:339, 1999.
[5] H. E. Huppert. Quantitative modeling of granular suspension flows. *Philos. Trans. R. Soc. London. Ser. A*, 356:2471, 1998.
[6] O. pouliquen, J. Delous, and S. B. Savage. Fingering in granular flows. *Nature*, 386:816, 1997.
[7] A. Acrivos, G. K. Batchelor, E. J. Hinch, D. L. Koch, and R. Mauri. Longitudinal shear-induced diffusion of spheres in a dilute suspension. *J. Fluid Mech.*, 240:651, 1992.
[8] D. Leighton and A. Acrivos. The shear-induced migration of particles in concentrated suspensions. *J. Fluid Mech.*, 181:415, 1987b.
[9] J. F. Richardson and W. N. Zaki. The sedimentation of a suspension of uniform spheres under conditions of viscous flow. *Chem. Eng. Sci.*, 5:65, 1954.
[10] B. Cook, A. Bertozzi, and A. Hosoi. Shock solutions for particle-laden thin films. *SIAM J. Appl. Math*, 68:760–783, 2008.
[11] J. Zhou, B. Dupuy, A. L. Bertozzi, and A. E. Hosoi. Theory for shock dynamics in particle-laden thin films. *Physical Review Letters*, 94:117803, 2005.
[12] B. Cook. Theory for particle settling and shear-induced migration in thin-film liquid flow. *Phys. Rev. E*, 78:045303, 2008.
[13] N. Murisic, B. Pausader, D. Peschka, and A.L. Bertozzi. Dynamics of particle settling and resuspension in viscous liquids. *J. Fluid Mech.*, 717:203–231, 2013.
[14] N. Murisic, J. Ho, V. Hu, P. Latterman, T. Koch, K. Lin, M. Mata, and A.L. Bertozzi. Particle-laden viscous thin-films on an incline: Experiments compared with a theory based on shear-induced migration and particle settling. *Physica D: Nonlinear Phenomena*, 204(20):1661–1673, 2010.
[15] S. Lee, A. Mavromoustaki, G. Urdaneta, K. Huang, and A.L. Bertozzi. Experimental investigation of bidensity slurries on an incline. *Granular Matter.*, 2014.
[16] T. Ward, C. Wey, R. Glidden, A. E. Hosoi, and A. L. Bertozzi. Experimental study of gravitation effects in the flow of a particle-laden thin film on an inclined plane. *Physics of Fluids*, 21:083305, 2009.
[17] C. Ancey, N. Andreini, and G. Epely-Chauvin. The dam-break problem for concentrated suspensions of neutrally buoyant particles. *J. Fluid Mech.*, 724:95–122, 2013.
[18] N. Grunewald, R. Levy, M. Mata, T. Ward, and A. L. Bertozzi. Self-similarity in particle laden flows at constant volume. *J. Eng. Math.*, 66:53–63, 2010.
[19] A. Mavromoustaki and A.L. Bertozzi. Hyperbolic systems of conservation laws in gravity-driven, particle-laden thin-film flows. *Journal of Engineering Math.*, 2014.
[20] L. Wang and A. L. Bertozzi. Shock solutions for high concentration particle laden thin films. *SIAM J. Appl. Math.*, 2014.
[21] M. Sever. *Distribution solutions of nonlinear systems of conservation laws*. Mem. Amer. Math. Soc., 2007.